Research Paper

A miniaturized selective laser melting device for *operando* X-ray diffraction studies

Samy Hocine[a,b], Steven Van Petegem[a], Ulrich Frommherz[c], Gemma Tinti[d], Nicola Casati[e], Daniel Grolimund[f], Helena Van Swygenhoven[a,b,*]

[a] *Photons for Engineering and Manufacturing, Paul Scherrer Institute, Forschungsstrasse 111, 5232 Villigen PSI, Switzerland*
[b] *Neutrons and X-rays for Mechanics of Materials, IMX, École Polytechnique Fédérale de Lausanne, Route Cantonale, 1015 Lausanne, Switzerland*
[c] *Engineering and Coordination, Paul Scherrer Institute, Forschungsstrasse 111, 5232 Villigen PSI, Switzerland*
[d] *SLS Detectors Group, Paul Scherrer Institute, Forschungsstrasse 111, 5232 Villigen PSI, Switzerland*
[e] *Materials Science Beamline, Paul Scherrer Institute, Forschungsstrasse 111, 5232 Villigen PSI, Switzerland*
[f] *MicroXAS Beamline, Paul Scherrer Institute, Forschungsstrasse 111, 5232 Villigen PSI, Switzerland*

ARTICLE INFO

ABSTRACT

We report on the development of a miniaturized device for *operando* X-ray diffraction during laser 3D printing. The printing chamber has a size of only $130 \times 135 \times 34$ mm^3 and is optimized to be installed at synchrotron beamlines. We describe the design considerations, details on the setup and the implementation at two different beamlines of the Swiss Light Source. Its capabilities are demonstrated by *ex situ* printing of complex shapes and *operando* X-ray diffraction experiments using Ti-6Al-4V powder. It is shown that the beamline characteristics have an important influence on the X-ray footprints of the microstructural evolution during 3D printing. From the intensity of the diffraction peaks, the evolution of the different phases can be followed during printing. Furthermore, the diffuse scattering signal provides information on the precise location of the laser beam on the sample and the scanning head settling time.

1. Introduction

Selective laser melting (SLM) is a well-known process category of the additive manufacturing (AM) family. It is a powder bed based technique, in which parts are built by selectively fusing the powder particles with a high-power laser source in a layer-by-layer fashion. Many processing parameters can be varied, such as laser power, scanning speed, layer thickness, hatch distance, printing strategies, powder size distribution, etc. By tweaking these multiple parameters, one can influence the resulting microstructure, and thus the physical properties of the final product [1–5]. Because of this multitude of parameters and the fact that some of them are inter-correlated, optimizing the processing window can be very time-consuming.

Simulations are emerging to accelerate the selection procedure. There exist many models that aim to gain deeper insight into the role of the different individual parameters and to predict the resulting microstructure [6–9]. However, the physical phenomena underlying the SLM process act on length and time scales that span multiple orders of magnitude. As a consequence, models can become very complex [10,11] and need input obtained by both *in situ* and post-processing characterization techniques.

In situ X-ray diffraction is a well-established technique to investigate the evolution of the microstructure in bulk materials during fast thermal processing. For instance, the precipitation kinetics during rapid solidification in Al-based alloys was studied by *in situ* small-angle X-ray scattering combined with laser-based heating [12]. Fast *in situ* X-ray diffraction was used to investigate phase transformations during fast cooling of a Ti-based alloy [13,14]. In such experiments, cooling rates are of the order of a few tens up to a few thousand degrees per second.

Thanks to the recent development of ultra-fast X-ray detectors and improvements at synchrotron beamlines, it is now possible to perform *in situ* X-ray diffraction and radiography experiments at time scales that are compatible with SLM processing, where heating/cooling rates of the order of 10^5-10^7 °C/s are achieved. In recent years, several fast *in situ* radiography experiments during laser-powder interaction have been performed [15–17]. These experiments require a particular setup that allows the X-ray beam to pass through the powder and solidified material. The powder is sandwiched between two plates that are transparent to X-rays. The distance between these two plates ranges from 0.3 to 0.5 mm. A laser beam positioned above the plates melts the top part

---

of the loose powder, whereas the X-ray beam impinges on the sample horizontally, providing a side view of the powder. These experiments provide information on the melt pool shape, and the formation of pores and sputters while printing a single track. However, such quasi-2D setups do not capture the 3D character of a conventional powder bed, and the full complexity of the layer scanning process. Furthermore, it does not allow to use complex scanning strategies.

To overcome these limitations, we have developed a miniaturized SLM device (MiniSLM) that is compatible with synchrotron X-ray diffraction. This allows performing ultra-fast, true *operando* X-ray diffraction while printing complex 3D structures under conditions that resemble very well those encountered in industrial SLM devices. The MiniSLM device was successfully used in an *in situ* study that demonstrated the influence of the length of the scanning vector on the resulting microstructure in Ti-6Al-4 V [18]. In this work, we detail the design and implementation of the MiniSLM device. We demonstrate its capabilities and discuss the influence of the synchrotron beamline characteristics on the X-ray footprints observed during *operando* X-ray diffraction.

2. MiniSLM design

2.1. Design considerations

The design of the MiniSLM device is largely based on conventional powder bed fusion devices that are commercially available. This includes key components such as 1) a build plate to act as a support for the printed part, mounted on a vertical piston to define the layer thickness, 2) a recoating system to deposit a new layer of powder and 3) a high-power laser source coupled to a scanning unit to selectively fuse the powder with the previously solidified layer. All this is confined in a printing chamber under inert gas atmosphere [19].

In order to use such a device at synchrotron beamlines, several constraints need to be considered. First, the incoming X-ray beam needs access to the powder bed and the divergent diffracted X-ray beam needs to be able to reach a detector placed outside the printing chamber. Therefore, X-ray transparent openings are needed on the printing chamber. Furthermore, the whole setup has to be transportable to be installed at a beamline for the experiment. The device itself has to fit on the beamline stage in between other beamline components. For instance, the distance between certain focusing optics, such as Kirkpatrick-Baez mirrors, and the focal plane can be of the order of 10-20 cm, which puts strong limitations on the maximum size of the printing chamber. The other SLM components, such as laser, controllers, etc; must fit around. The SLM device needs to be controlled from outside the experimental hutch, which is not accessible during an X-ray experiment. Finally, the synchrotron beamline and laser must be synchronized with high accuracy.

2.2. Detailed setup

For the X-ray beam to have access to the powder bed, the complete device needs to be tilted. This is shown schematically in Fig. 1. The inclination angle should be such as the powder does not flow from the build plate. A powder starts flowing on an inclined surface when the angle exceeds the angle of repose, which is defined by the angle at the base of the cone formed by the powder when poured on a flat surface. For most powders this angle is usually above 20° [20]. Therefore, the device is mounted on a heavy load tilting stage (Huber, Germany) that allows a rotation of ± 20° around a horizontal axis.

The device has a height of 520 mm and its lateral dimensions are 280 mm and 260 mm, parallel and perpendicular to the direction of the X-ray beam, respectively. The overall weight (including the tilting stage) is 25 kg. Figs. 2–4 describe in detail the different parts of the device. The components are labelled by numbers and explained in the following paragraphs. The printing chamber includes two openings at
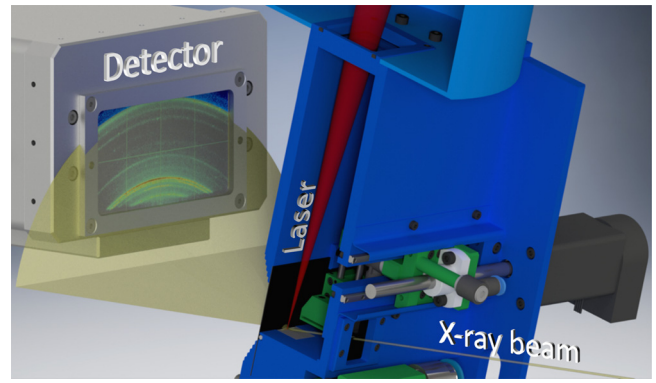

Fig. 1. Diffraction geometry during an *operando* measurement. The X-ray beam enters the printing chamber through the glassy carbon window at the back of the machine, while the laser enters at the top. They both interact with the powder on the build plate. The diffracted X-ray beam forms a diffraction cone that is collected by a high-speed detector in front of the machine.

the back (Fig. 2 - (2)) and front (Fig. 2 - (3)) for, respectively, the entrance and exit of the X-ray beam. The incoming beam enters the backside through a 100 μm glassy carbon window (HTW, Germany), interacts with the build stage area where the printing is done and exits through a 500 μm thick window, also made of glassy carbon. Glassy carbon was selected because of its high transparency to hard X-rays and opacity to visible and infrared light. Thus, *operando* diffraction experiments can be performed without letting the laser beam escape the chamber and damage the surrounding equipment at the beamline. The width and height of the entrance window were chosen such that the X-ray beam has access to the whole build plate surface when the machine is tilted to up to 20°. The width and height of the exit window were chosen such that diffraction angles up to 70° can be achieved.

The printing chamber constitutes the core of the MiniSLM device. The build plate (Fig. 3 – (10)) has a surface area of 12 x 12 mm^2 and is mounted on a high precision motorized vertical stage (Fig. 2 – (4)) with a step resolution of 21 nm (8MVT40-13-1, Standa Ltd, Lithuania) and a travel range of 12 mm. However, the total build height is restricted to about 5 mm depending on the powder quality, layer thickness and losses during the recoating. Due to the lack of space inside of the chamber, it was not possible to dimension the recoater big enough to ensure the complete filling of the build volume.

A custom-made zirconia ceramic holder serves as a support and link between the plate and the motorized stage (Fig. 3 – (11)). Inside of the ceramic holder, a silicon-nitride resistive heater (Bach RC, Germany, Fig. 3 – (12)) is placed directly in contact with the build plate (Fig. 3 – (10)). The contact surface is relatively small (1.5 x 7 mm^2) but it can reach up to 500 °C. A fine gage unsheathed type K thermocouple (OMEGA Engineering, INC., US, Fig. 3 – (13)), is placed under the resistor. The temperature is controlled by a conventional PID closed-loop control protocol. A silicon joint is surrounding the plate (Fig. 3 – (14)) in order to prevent powder from falling in the clearance gap between the ceramic holder and the frame of the machine. The whole assembly is held together with a screw (Fig. 3 – (15)), using the build plate as clamp to press everything together. In the current design, the maximum temperature that can be reached on top of the baseplate is only 100 °C. The most important factors that prevent reaching higher temperatures are: 1) loss of contact during heating because of different thermal expansion of the various components, 2) the small size of the ceramic heater compared to the size of the baseplate and 3) heat losses.

The powder delivery system is a hopper-based design with a doctor blade [19]. The powder is stored in a funnel-like cavity (Fig. 3 – (16) and Fig. 4 – (21), in green). Prior to recoating, the build plate is moved down to a height corresponding to one layer thickness. This creates a gap between the top of the plate and the frame of the machine. A motor-spindle assembly (Igus® Schweiz GmbH, Fig. 2 – (5)) drives the
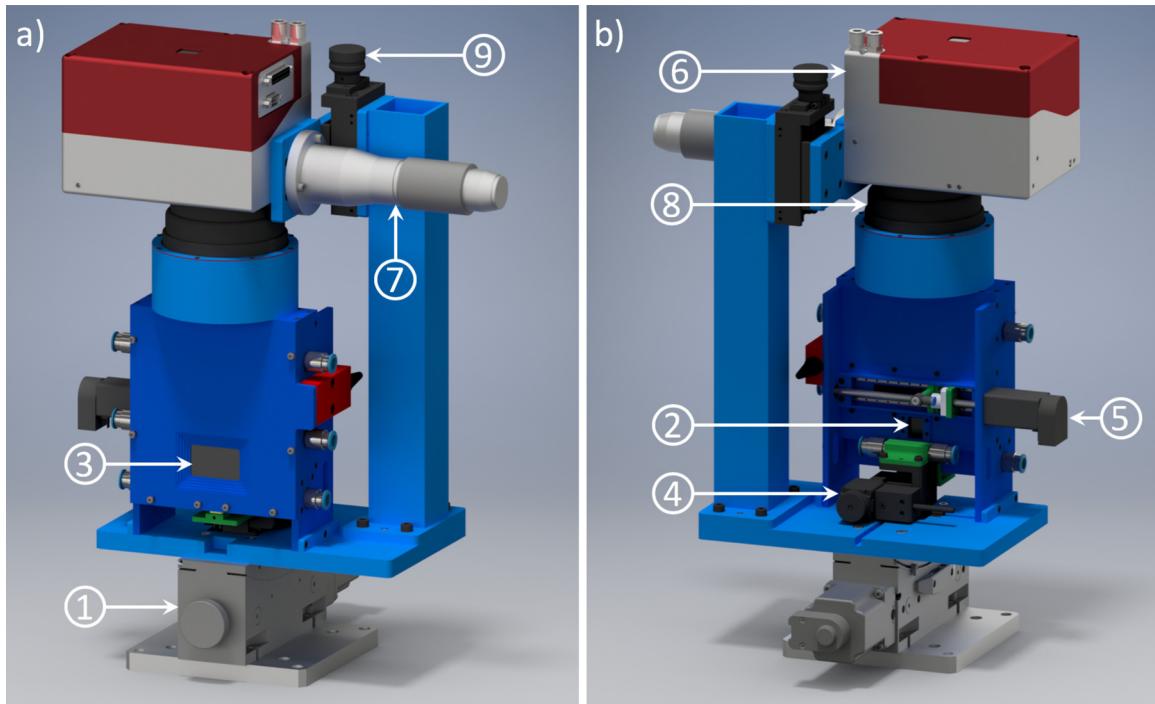
Fig. 2. Rendered 3D model of the MiniSLM with front view (a) and back view (b). 1) tilt stage, 2) entrance window, 3) exit window, 4) motor build stage, 5) motor recoater, 6) scanning head, 7) laser collimator, 8) F-theta lens, 9) vertical stage to change focal length. More details on the different components are given in the text.

recoating system above the newly formed gap, while the horizontality of the movement is ensured by two miniature linear guides (Chieftek Precision Co., Ltd, Taiwan). The powder falls in the gap during the first passage of the recoater, and the excess of powder is scrapped by the blade on its way back, creating the freshly deposited layer. The recoater was designed so that no excessive force is applied on the powder bed during the recoating process: when setting up the recoater, four springs (Fig. 4 – (22)) ensure that the silicon blades are in contact with the base of the machine before locking it into position with two screws (Fig. 4 –

(23)) to avoid any vertical movements during the recoating.

It is known that flowability of metallic powders can be bad [21]. This is particularly critical for gravity-based recoating systems, since the powder tends to stick on the walls or agglomerate at the bottom of the funnel. To overcome this, a vibration system has been installed on the beam holding the recoater (Seeed Studio, China). The vibration is activated during the recoating process in order to enhance the flowability of powder.

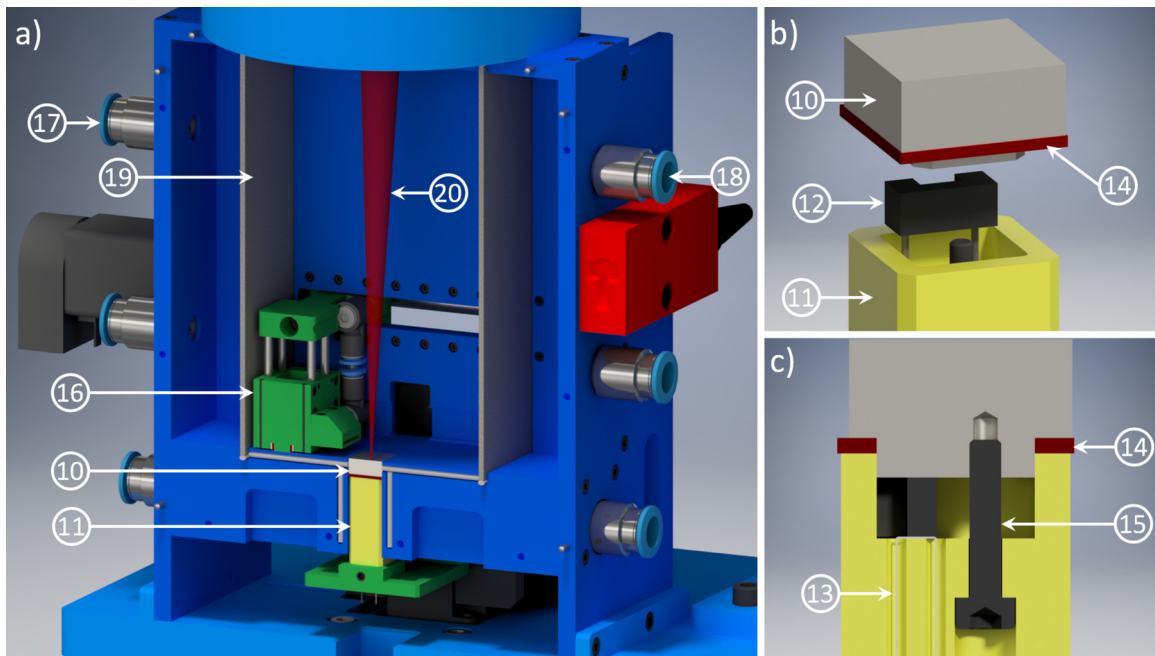The chamber is continuously flushed with high purity argon gas

Fig. 3. a) 3D rendering of the printing chamber of the MiniSLM, b) split view of the ceramic heater, c) cross-section of the ceramic heater. 10) build plate, 11) ceramic holder, 12) heater, 13) thermocouple, 14) sealing, 15) clamping screw, 16) recoater, 17) gas inlet, 18) gas outlet, 19) steel filters, 20) laser beam. More details on the different components are given in the text.
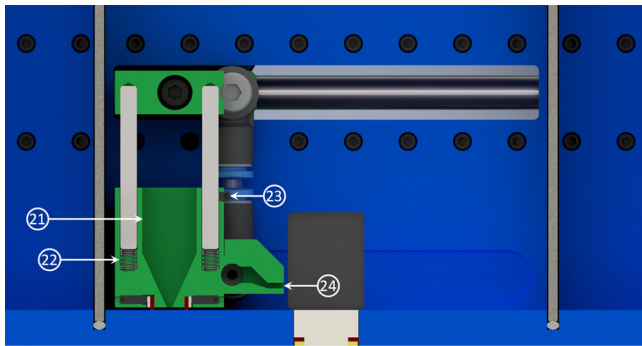
Fig. 4. Cross section of the printing chamber showing the recoater design. 21) recoater funnel, 22) spring, 23) screws, 24) gas nozzle. More details on the different components are given in the text.

(99.998% Ar, Carbagas) from the gas inlets (Fig. 3 –(17)). A vacuum pump (KNF Neuberger AG) is connected to the outlets (Fig. 3 – (18)) to ensure a unidirectional flow. Additionally, a local argon flow is generated above the powder bed through a nozzle mounted on the recoater (Fig. 4 – (24) in green). The input, output and nozzle flows are controlled with manual flowmeters (Vögtlin Instruments AG). The flow of the inlet is set slightly higher than that of the outlet, which creates a small overpressure in the chamber. This avoids oxygen contamination from the outside atmosphere. A small oxygen monitoring module (Pewatron AG) monitors the oxygen level at the outlet with an 0.2% accuracy below 10% oxygen. Different sets of filters are placed along the inert gas circuit to sieve ejected particles generated during printing. In the chamber, after the input and before the output, 1 μm opening stainless steel filters (TWP Inc., US, Fig. 3 – (19)) are mounted. For sub-micron particles, an 0.2 μm opening PTFE hydrophobic filter (Merck & Cie, CH) is placed before the oxygen sensor to protect it, and a simple water-based filter is placed after the pump to catch any residual particles.

A high-energy laser beam (redPOWER, SPI Lasers Ltd, UK) with maximum power of 500 W is directly collimated as a parallel Gaussian beam (ø9.6 mm at $1/e^2$, Fig. 2 – (7)) into a 2-axis deflection scanning unit (SuperScan III, Raylase GmbH, Germany, Fig. 2 – (6)). Two fused silica mirrors galvanometer (di-electric coating, reflectivity > 99.5% at 1064 nm) pilot the laser beam in the two horizontal directions of the printing area. The laser beam is focused through a F-Theta lens (Sill Optics, Germany, Fig. 2- (8)) to a minimum spot size of 25 μm at the focal plane of the lens. Larger spot sizes can be achieved by defocussing using a micrometric precision linear stage (OWIS LT 60-25, Fig. 2 – (9)).

The laser beam (Fig. 3 – (20)) enters the printing chamber through a 500 μm thick fused quartz window (UQG Optics, UK) with an anti-reflection coating (R < 0.50%) on both sides. Shielding elements are placed along the laser beam path, between the lens and the chamber window, to protect the user from possible back reflections. The whole setup (laser, scanning unit and printing chamber) is cooled down with a closed-loop air-water exchanger chiller (Termotek GmbH, Germany). The laser and chiller are mounted on a standard 19 inches rack housing on wheels, to facilitate transport.

The complete setup is managed by a single computer. The laser and scanning unit are steered via a SP-ICE-3 board that can be controlled by the WeldMARK software (Raylase GmbH, Germany). This an engraving software that offers different scanning strategies: unidirectional and bidirectional raster scanning (with or without meander) and cross hatch scanning. The scanning vector can be rotated at any angle value within the printing plane. All the motors are steered with USB controllers (Standa Ltd, Lithuania). An in-house written LabVIEW-based software package was developed to control and synchronize all components. The communication between WeldMARK and LabVIEW is achieved over a standard ActiveX communication protocol. One of the advantages of this method is that LabVIEW can call independently any of the

functions embedded in WeldMARK, which makes it very flexible. For instance, it allows to print complex 3D structures or combine various scanning strategies. During *operando* measurements the control computer is placed inside the experimental hutch and remotely controlled from the control room.

3. Results

3.1. Material characterization

The material investigated in this work is Ti-6Al-4V (wt.%), an alloy widely used in the aerospace and medical industries because of its low mass density, high corrosion resistance and biocompatibility [22]. This alloy is often used in additive manufacturing because of its stable processability and good mechanical properties [3]. It undergoes an α→β→liquid transformation when heated up, and for cooling rates higher than 410 °C/s, it will solidify into an α' martensitic phase [23]. During SLM processing, the cooling rates are usually in the order of 10^5-10^6 °C/s due to the fast scanning speeds. As a result, the obtained microstructure primarily results in fine acicular α' martensite laths, arranged in columnar prior-β grains growing along the build direction [24,25]. A strong texture is formed in the printed part since those prior-β grains grow epitaxially along the [001] crystallographic direction [26]. This type of microstructure is typical of SLM processing, but presents different kinds of defects such as twin boundaries and dislocations formed within the columnar prior-β grains [27]. Such microstructure has poor strength and ductility [1], therefore a lot effort is put into post-treatment to decompose the α' martensite into an α + β microstructure [28].

In the framework of this experiment, the substrates were machined from standard commercial Ti-6Al-4V alloy. The powder used for the printing is a Ti-6Al-4V ELI (extra low interstitial, grade 23), gas atomized, with spherical particle shape (LPW Technology LTD, Widnes, United Kingdom).

3.2. Ex situ 3D printing

Experimental time at synchrotron beamlines is very restricted. Therefore, it is important to narrow down the range of laser processing parameters prior to the *operando* experiments. The main selection criteria are sample density and surface roughness. High sample density is usually required for optimal mechanical properties of the built part. To measure the sample density, an image of the sample cross-section perpendicular to the build direction is taken after polishing. The picture is then post processed with the software ImageJ into a black (pores) and white (metal) image. The relative density is determined from the ratio of these two quantities. For the Ti-6Al-4V samples presented in this work the best-obtained relative density was 99.8%.

The surface roughness needs to be kept low when working in reflection mode. High surface roughness results in an angular dependence of the diffracted intensity. Furthermore, when the roughness changes during printing, the intensities may change dramatically. The surface roughness is inspected by SEM imaging (Fig. 5a-d) of the top and side surfaces of the sample and is judged "good" when the melt tracks are clearly visible and homogeneous, without large irregularities (Fig. 5c and d). The selection criterion for the *operando* measurements was based on the melt track quality of the top surface only.

The MiniSLM has the capability of printing complex 3D sample based on CAD drawings. The software Slic3r [29] is used to slice an STL file ("Standard Triangle Language" or "Standard Tessellation Language") into layers with a defined thickness. These are exported into an SVG file (Scalable Vector Graphics), which can be used in the WeldMARK environment, and thus also in our in-house written software. The 3D part is printed by loading each slice at the corresponding layer height (Fig. 5e and f). Fig. 5f shows a 3D print of the well-known Matterhorn mountain.
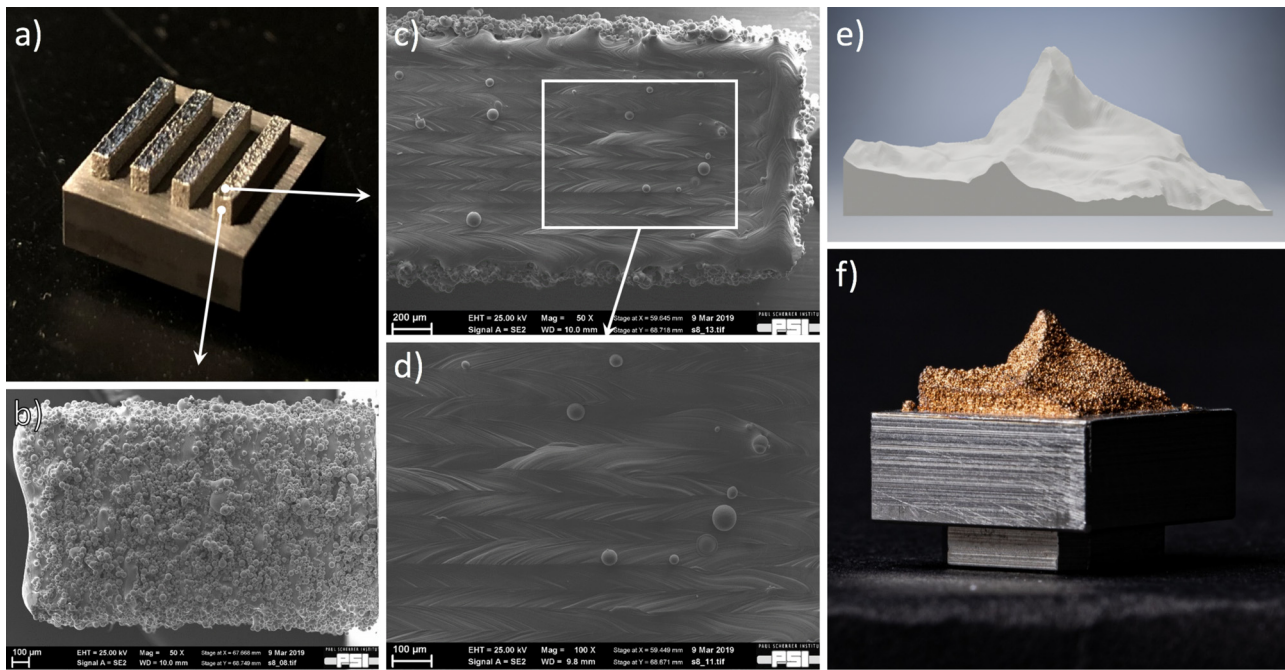
Fig. 5. 3D printed structures: a) e*x-situ* sample made of Ti-6Al-4 V for surface roughness observation. The sample with the best surface roughness is presented, with the following printing parameters: 100 µm laser spot diameter, 250 W laser power, 600 mm/s scanning speed and 60 µm hatch distance, b) roughness of side surface, c) roughness at top surface d) zoom, e) STL model used for the Matterhorn 3D printing, f) 3D printed model made of CuSn8.

3.3. Operando X-ray diffraction

3.3.1. Detector requirements

The X-ray detector is a crucial component for *operando* measurements. During SLM processing the local microstructure changes very fast because of high laser scanning speeds (of the order of 1 m/s) and high heating/cooling rates (up 10^6 °C/s). In order to capture these phenomena a fast X-ray detector with sub-millisecond time resolution is crucial. This, in turn, requires an X-ray beam with high brilliance, in order to acquire diffraction spectra with sufficient statistics in each single frame. Furthermore, the background noise needs to be kept as low as possible. This can be achieved by X-ray detectors with energy threshold. X-ray detectors that work at very high frame rates usually have limited storage capacity. It is therefore important to properly synchronize the detector with the laser operation.

For the experiments reported in this work an in-house developed EIGER detector [30] was used. It is an ultrafast single photon counting hybrid detector with maximum storage capacity of 30'000 frames in 4-bit mode. The detection module has an area of approximately 8×4 cm^2 and contains 500'000 pixels, each with a size of 75×75 µm^2. The detector was operated at a frame rate of 20 kHz during 1 s. The exposure time of a single frame was 45 µs, and the lower energy threshold was set to 8 keV.

3.3.2. Scattering geometry

The MiniSLM can be used in both transmission and reflection mode. In transmission mode (Fig. 6a and b), the X-ray beam is aimed near the edge of the build plate and goes through the sample, hence the term "transmission". In the reflection mode (Fig. 6c and d), the X-ray beam is located further away from the edge. Here, only the reflected part of the beam with diffraction angles larger than the tilt of the machine can reach the detector. In what follows we restrict to results obtained in reflection mode.

Fig. 7 illustrates the scattering geometry in reflection mode during laser operation. The penetration depth of the X-ray beam can be tuned by adapting X-ray beam energy and/or tilt angle of the device. It should be noted that the latter influences the size of the area on the sample illuminated by the X-ray beam. This area is determined by the projection of the X-ray beam on the tilted surface. Smaller tilt angles result in a lower penetration depth but a larger projected area, which reduces the spatial resolution of the measurements. For the experiments presented in this work a beam energy of 12 keV and tilt angle of 15° was used. This limits the penetration depth to a few tens of micrometers in Ti-6Al-4V.

3.3.3. Data analysis

During the *operando* measurements, up to 20'000 2D images were acquired for each printed layer. These images were reduced to 1D patterns by azimuthal integration using the Bubble software package [31]. This package is based on pyFAI, a well-established python library for fast powder integration [32].

Fig. 8a displays a representative result obtained after printing a single layer. The data is presented as an intensity versus diffraction angle and time plot by stacking the individual diffraction patterns. Fig. 8b shows the diffraction patterns recorded prior to printing and at t = 320 ms, for which most of the area illuminated by the X-ray beam is converted to the β-phase. In principle, the diffraction peaks can be analysed by single peak fitting, which provides values for integrated intensity, peak position and width. However, because of texture formation, phase transformation or limited grain sample statistics, the intensity of the diffraction peaks is not always sufficient to perform reliable peak fitting. In that case, the first and second moment of the peaks are calculated, from which the center-of-mass and variance are obtained [33]. The evolution of the integrated intensity provides information on the phase evolution during printing. The peak position (or center-of-mass) is mainly influenced by temperature and residual stresses. In previous work [18] the temperature evolution in both the α- and β-phase were obtained under the assumption that peak position is mainly affected by thermal expansion.

It is also interesting to investigate the diffuse scattering in the regions between the diffraction peaks, as indicated by the arrow in Fig. 8b. The intensity of the diffuse scattering is strongly affected by thermal diffuse scattering and contributions from the liquid melt pool. The latter gives rise to a sharp increase in diffuse scattering, as
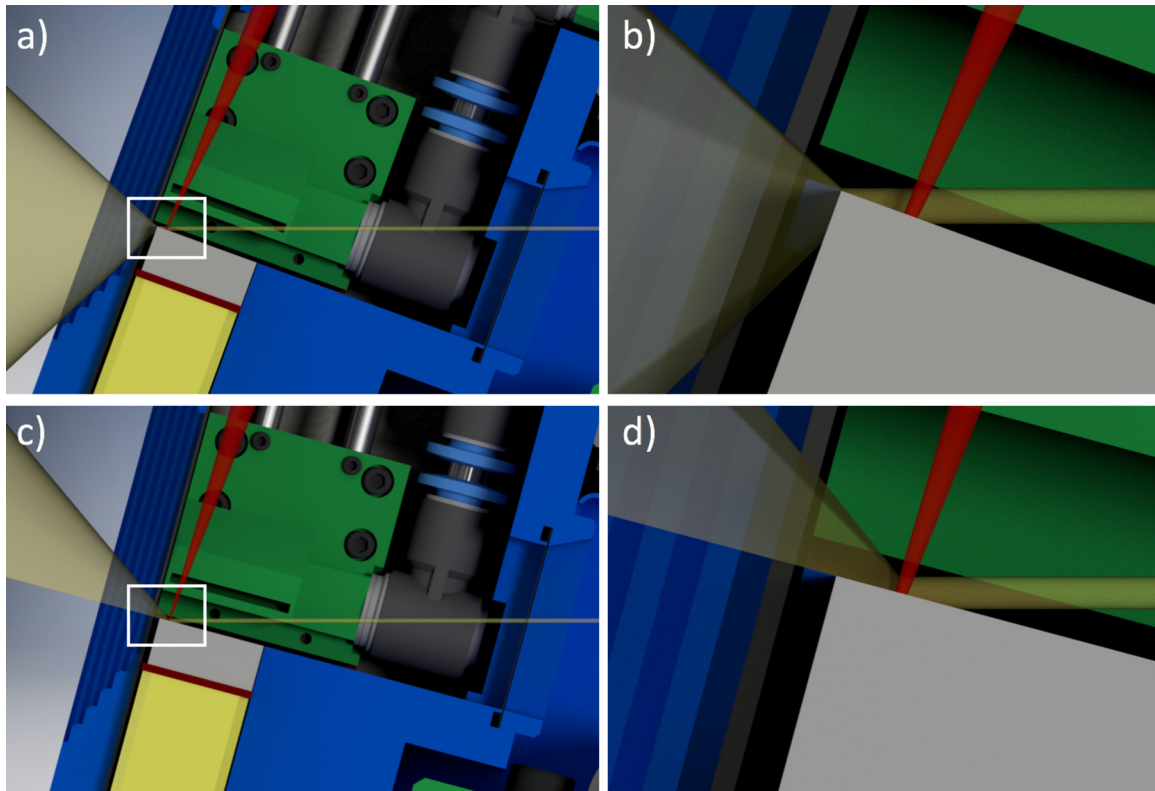
Fig. 6. 3D rendered cross section of the machine, illustrating the configuration for transmission (a,b) and reflection (c,d) mode.
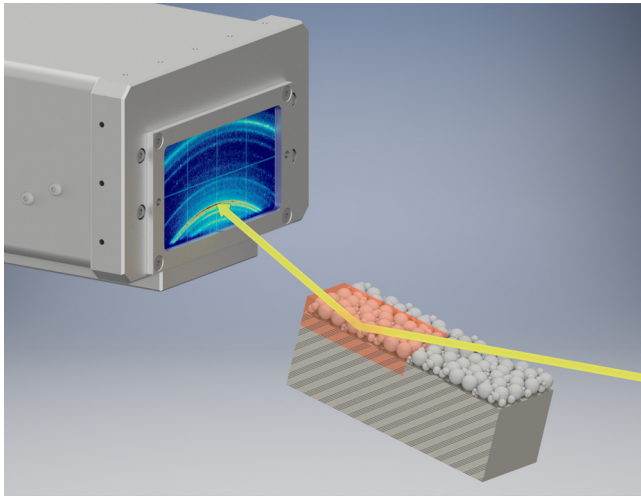

Fig. 7. Schematic of the scattering geometry in reflection mode, showing the X-ray beam, a cross-section of the powder bed and the X-ray detector. The X-ray beam has a fixed position on the power bed, which is tilted by 15˚. The area scanned by the laser is highlighted in red.

demonstrated in section 3.3.4. For this work, the diffuse scattering signal is obtained by summing the integrated intensity between $(01.0)_\alpha$ - $(00.2)_\alpha$ ($24.2° \leq 2\theta \leq 25.2°$) and $(01.1)_\alpha – (01.2)_\alpha$ ($28° \leq 2\theta \leq 34°$).

3.3.4. Influence of beamline characteristics

The synchrotron beamline characteristics have an important influence on the X-ray diffraction footprints of the microstructural evolution during printing. This is illustrated by comparing the results from *operando* experiments performed at MicroXAS and MS, two hard X-ray beamlines located at the Swiss Light Source. Fig. 9 illustrates the two different setups at the respective beamlines. The main difference

between these two beamlines is the beam size. At the MS beamline, the X-ray beam was focused down to a size of 130 x 60 μm^2 (horizontal x vertical), which corresponds to an illuminated area A_x = 130 x 230 μm^2 on the sample surface. The MicroXAS beam line exhibits additional focusing optics (Kirkpatrick-Baez mirrors) close to the sample position. This was used to focus down the X-ray beam to 80 x 35 μm^2, resulting in A_x = 80 x 140 μm^2.

Table 1 lists the processing parameters used for the experiments. At each beamline, samples with an area of 2 x 2 mm^2 were printed. The X-ray beam was positioned in the middle of the printed area. The laser scanning starts at the outer edge and covers the complete scanned area in a bi-directional fashion. As the hatch distance is smaller than the vertical dimension of A_x, the laser beam passes multiple times through the area illuminated by the X-ray beam.

Recently, it was shown that while printing consecutive Ti-6Al-4V lines with a scan vector of 8 mm and parameters given in Table 1, the center of the sample has enough time (> 13 ms) to cool down to temperatures where the β-phase is not stable anymore. As a consequence, the microstructure exhibits multiple short transitions of a few milliseconds between α and β [18]. In contrast, when printing with a scan vector of 2 mm, the center of the sample remains above the β-transition temperature while printing multiple consecutive lines. As a consequence, by reducing the length of scanning vector the high-temperature β-phase exists over a longer time and exhibits lower cooling rates. This results in larger prior-β grain sizes and different morphology of the α' microstructure [18].

Fig. 10a and b display the evolution of the integrated intensities of the $(01.1)_\alpha$- and $(002)_\beta$-phase (respectively blue and red curves) together with the intensity of the diffuse scattering (yellow background) as a function of time while printing a single layer of the 2 x 2 mm^2 sample, measured at the MicroXAS and MS beamlines, respectively. Note that the intensity of each phase is normalized to its maximum.

The results from the MS beamline are qualitatively similar to the ones obtained at MicroXAS. There are, however, a few key differences that are related to the significantly larger size of A_x. First, the signals at
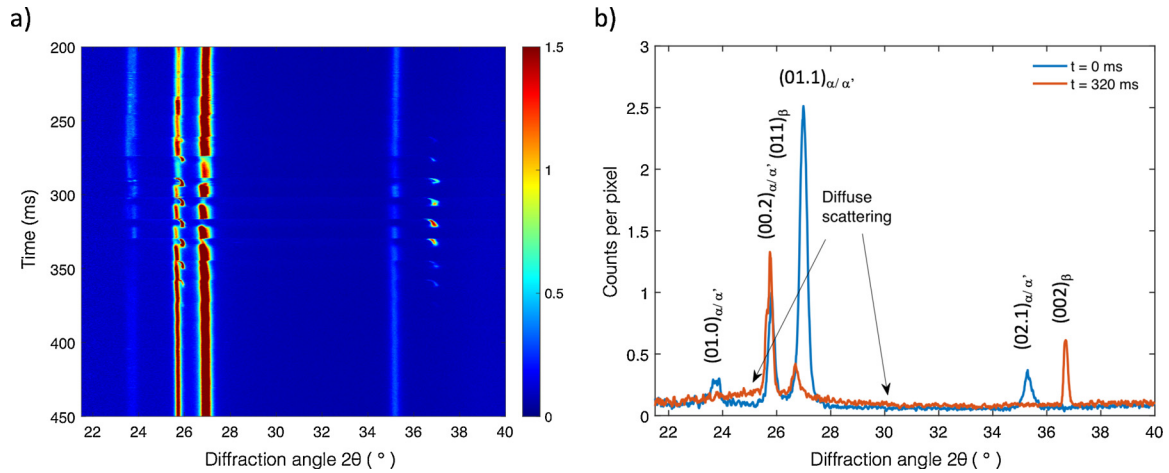
Fig. 8. a) Evolution of diffraction patterns during printing of a single layer, shown as an intensity vs. diffraction angle and time waterfall plot. Note that the color scale was capped at 1.5 counts per pixel for visibility reasons, b) indexed individual diffraction patterns recorded prior to printing and at time t = 320 ms.

MS are noisier, even though the intensity of the incoming X-ray beam is comparable to the one of MicroXAS. This may be related to the spatter created during printing. The X-ray beam area at MS is about three times larger compared to MicroXAS, resulting in significantly higher chance for interaction with spatter. Furthermore, the observed fluctuations of the intensities may be affected by moving powder caused by denudation and entrainment effects. Second, the α-phase never disappears at MS because there is always a part of A_x where the temperature is below the β-transition temperature. Finally, the intensity of the diffuse scattering signal from the melt pool is less pronounced and reflects less the passage of the laser. The major advantage of using a larger X-ray beam lies in a better grain sampling statistics of the solid phase.

To obtain a maximum of information on the interaction of laser and material, the size of the X-ray spot should be similar as that of the laser spot. Fig. 11a shows a zoom of the region indicated by the black dashed lines in Fig. 10a. Fig. 11b displays a schematic that shows at particular times (numbered in Fig. 11a) the relative position of the laser, X-ray beam, melt pool and the region that exhibits the β-phase. This schematic is inspired by the results from finite element simulations, as shown in [18].

Printing starts at t = 0 ms, where the laser beam is far away from A_x and only the α-phase is visible. Between t = 47 ms and t = 66 ms, the α-phase gradually disappears in a step-like manner. Here, part of A_x is transformed to the β-phase, as shown schematically in Fig. 11b for position 1. At t = 58 ms, the diffuse scattering exhibits a short increase

Table 1
Processing parameters.

Laser characteristics	
Spot size	100 μm
Power	250 W
Scanning speed	600 mm/s
Hatch distance	60 μm
Scanning strategy	Bi-directional
Powder bed	
Base plate material	Ti-6A-4V
Pre-heating temperature	70 °C
Layer thickness	30 μm

in intensity. This is the signature of the melt pool that passes partly through A_x (see also position 2 in Fig. 11b). At t = 66 ms, the α-phase has completely disappeared. During the next transition, the melt pool passes through the center of A_x (position 3). The melt pool passes 6 times through A_x, as witnessed by the 6 spikes in the diffuse scattering. The last passage occurs at t = 78 ms. Beyond this point, the laser beam does not overlap anymore with A_x. The temperature in A_x decreases, but remains above the β-transition temperature for another 40 ms. At t = 120 ms the β-phase gradually transforms into the α-phase. At t = 135 ms, printing has finished, after which the temperature in A_x keeps on decreasing and the little remaining β-phase transforms further into α. Finally, the microstructure exhibits no β-phase anymore.
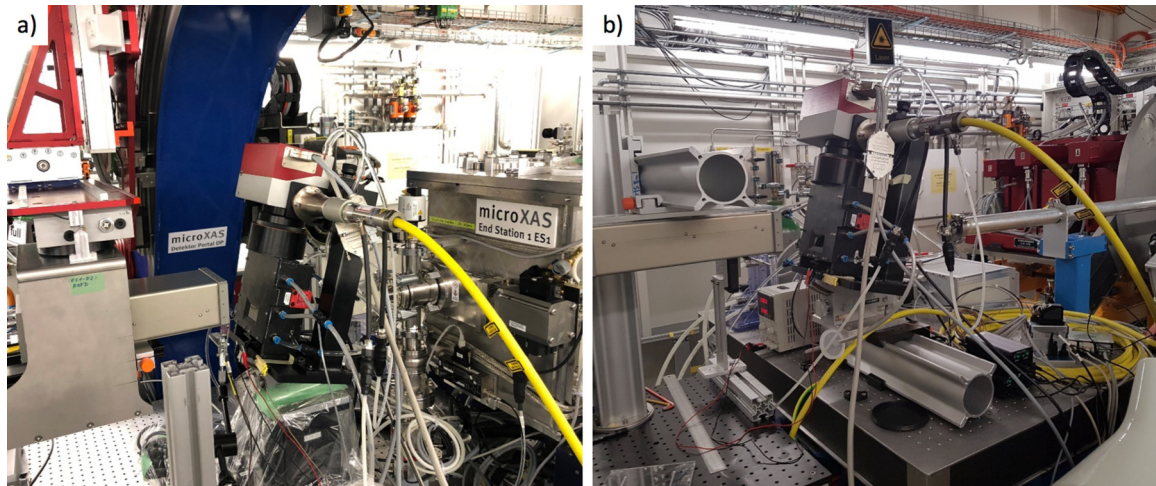

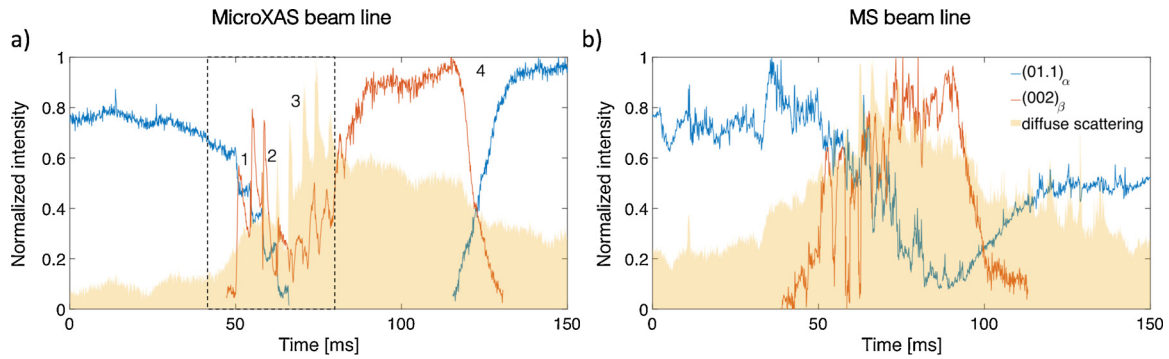**Fig. 9.** The MiniSLM device mounted at a) MicroXAS and b) MS beamlines.

Fig. 10. Comparison of the normalized integrated intensities of the $(01.1)_\alpha$- and $(002)_\beta$-phase and intensity of the diffuse scattering as a function of time for the 2 x 2 mm^2 sample printed at a) MS and b) MicroXAS. The intensity of each phase is normalized to its maximum.

Note that strong variations in intensity of the β-phase are observed, especially in the first lines when α starts disappearing, which probably can be assigned to the fact that only limited number of grains are in diffraction conditions. For instance, after an initial increase in the overall intensity, the β-phase exhibits an unexpected minimum intensity between t = 60 ms and t = 80 ms. In contrast, at MS the overall shape of the intensity of the β-phase exhibits a more gradual increase (Fig. 10b).

3.3.5. Scanning head settling time

From the signal of the diffuse scattering, the time to print a single track can be deduced and compared to the theoretical value. For this purpose, samples were printed with a scan vector of 8 mm and scanning speeds varying between 200 mm/s and 800 mm/s. The average duration of the single tracks was determined by averaging the time between the rising edges of the diffuse scattering signals. They are listed in Table 2 and compared to the theoretical values. Interestingly, the difference between the experimental and theoretical duration is independent of the scanning speed. This difference is due to the settling time: the time needed by the mirrors of the scanning head to move from the end of one track to the start of the next one. During this time the laser is switched off and the melt pool at the edge of the sample cools down. Note that a bi-directional scanning strategy was used for these measurements. In case of other scanning strategies, such as uni-directional scanning, this settling time will be different. The experimental determination of the settling time is of importance for simulations that aim to reproduce the temperature evolution while printing.

4. Conclusions

A new miniaturized device for *operando* X-ray diffraction during laser 3D printing was developed. Its design is based on the functionalities of commercially based SLM devices with the additional

Table 2
Experimental t_{exp} and theoretical duration t_{theo} to print a single 8 mm track as a function of scanning speed.

Speed (mm/s)	t_{exp} (ms)	t_{theo} (ms)	Δt (ms)
200	40.61	40	0.61
400	20.58	20	0.58
600	13.95	13.33	0.62
800	10.65	10	0.65

requirement that it can be implemented at synchrotron X-ray beamlines. Its reduced size makes it portable and enables the testing of powder that are newly developed for SLM purposes, since only a small volume is needed to print samples. Thanks to its software flexibility, it is possible to print CAD designed shapes to investigate sample geometry effects.

The device was successfully tested at different beamlines of the Swiss Light Source using Ti-6Al-4 V powder. It is shown that the beamline characteristics have an important influence on the X-ray footprints of the microstructural evolution during 3D printing. Taking these characteristics into account, the output of an *operando* experiment can provide data that can be used to validate computational simulations. From the intensity of the diffraction peaks, the evolution of the different phases can be followed during printing. The diffuse scattering signal provides information on the precise location of the laser beam on the sample and the laser settling time.

CRediT authorship contribution statement

Samy Hocine: Conceptualization, Methodology, Software, Formal analysis, Investigation, Writing - original draft, Writing - review & editing, Visualization. **Steven Van Petegem:** Conceptualization, Methodology, Software, Formal analysis, Investigation, Writing -
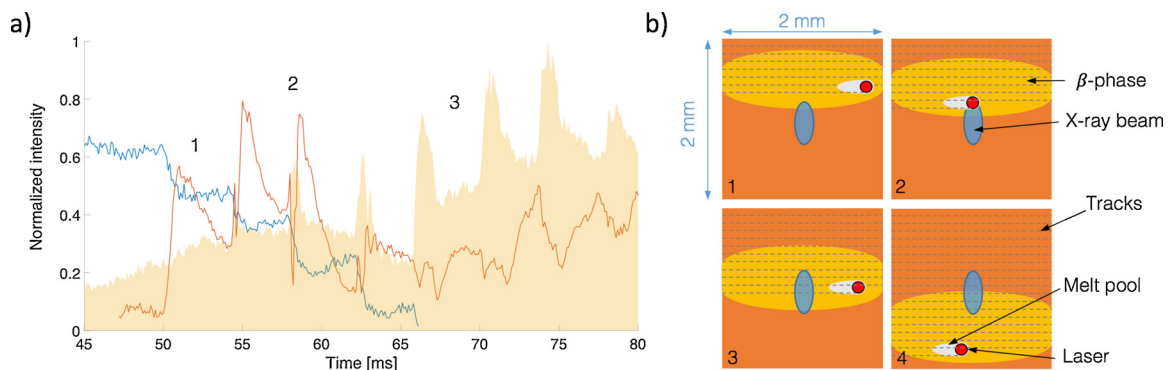

Fig. 11. a) Zoom in black dashed area in Fig. 10a, b) corresponding schematic showing the relative position of X-ray beam (blue), laser spot (red), melt pool (white) and β-phase (orange) at different times during printing, as indicated by the numbers Fig. 10a and 11a. The dashed lines represent the previously printed tracks.

Declaration of Competing Interests

The authors declare that they have no known competing financial interests or personal relationships that could have appeared to influence the work reported in this paper.

Acknowledgements

References

[1] J.J. Lewandowski, M. Seifi, Metal Additive Manufacturing: A Review of Mechanical Properties, Annu. Rev. Mater. Res. 46 (2016) 151–186, https://doi.org/10.1146/annurev-matsci-070115-032024.

[2] J.H. Martin, B.D. Yahata, J.M. Hundley, J.A. Mayer, T.A. Schaedler, T.M. Pollock, 3D printing of high-strength aluminium alloys, Nature 549 (2017) 365–369, https://doi.org/10.1038/nature23894.

[3] S. Liu, Y.C. Shin, Additive manufacturing of Ti6Al4V alloy: A review, Materials & Design. 164 (2019) 107552, , https://doi.org/10.1016/j.matdes.2018.107552.

[4] T. Scharowsky, A. Bauereiß, C. Körner, Influence of the hatching strategy on consolidation during selective electron beam melting of Ti-6Al-4V, Int J Adv Manuf Technol. 92 (2017) 2809–2818, https://doi.org/10.1007/s00170-017-0375-1.

[5] Z. Mao, D.Z. Zhang, P. Wei, K. Zhang, Manufacturing Feasibility and Forming Properties of Cu-4Sn in Selective Laser Melting, Materials. 10 (2017) 333, https://doi.org/10.3390/ma10040333.

[6] J. Beuth, J. Fox, J. Gockel, C. Montgomery, R. Yang, H. Qiao, E. Soylemez, P. Reeseewatt, A. Anvari, S. Narra, N. Klingbeil, Process mapping for qualification across multiple direct metal additive manufacturing processes, (2013), pp. 655–665.

[7] Q. Zhang, J. Xie, Z. Gao, T. London, D. Griffiths, V. Oancea, A metallurgical phase transformation framework applied to SLM additive manufacturing processes, Materials & Design. 166 (2019) 107618, , https://doi.org/10.1016/j.matdes.2019.107618.

[8] M. Markl, C. Körner, Multiscale Modeling of Powder Bed–Based Additive Manufacturing, Annual Review of Materials Research. 46 (2016) 93–123, https://doi.org/10.1146/annurev-matsci-070115-032158.

[9] P. Tan, F. Shen, B. Li, K. Zhou, A thermo-metallurgical-mechanical model for selective laser melting of Ti6Al4V, Materials & Design. 168 (2019) 107642, , https://doi.org/10.1016/j.matdes.2019.107642.

[10] L.-X. Lu, N. Sridhar, Y.-W. Zhang, Phase field simulation of powder bed-based additive manufacturing, Acta Materialia. 144 (2018) 801–809, https://doi.org/10.1016/j.actamat.2017.11.033.

[11] T. Keller, G. Lindwall, S. Ghosh, L. Ma, B.M. Lane, F. Zhang, U.R. Kattner, E.A. Lass, J.C. Heigel, Y. Idell, M.E. Williams, A.J. Allen, J.E. Guyer, L.E. Levine, Application of finite element, phase-field, and CALPHAD-based methods to additive manufacturing of Ni-based superalloys, Acta Materialia. (2017), https://doi.org/10.1016/j.actamat.2017.05.003.

[12] P. Schloth, J.N. Wagner, J.L. Fife, A. Menzel, J.-M. Drezet, H. Van Swygenhoven, Early precipitation during cooling of an Al-Zn-Mg-Cu alloy revealed by in situ small angle X-ray scattering, Appl. Phys. Lett. 105 (2014) 101908, , https://doi.org/10.1063/1.4894768.

[13] C. Kenel, D. Grolimund, J.L. Fife, V.A. Samson, S. Van Petegem, H. Van Swygenhoven, C. Leinenbach, Combined in situ synchrotron micro X-ray diffraction and high-speed imaging on rapidly heated and solidified Ti–48Al under additive manufacturing conditions, Scripta Materialia. 114 (2016) 117–120, https://doi.org/10.1016/j.scriptamat.2015.12.009.

[14] C. Kenel, P. Schloth, S.V. Petegem, J.L. Fife, D. Grolimund, A. Menzel, H.V. Swygenhoven, C. Leinenbach, In Situ Synchrotron X-Ray Diffraction and Small Angle X-Ray Scattering Studies on Rapidly Heated and Cooled Ti-Al and Al-Cu-Mg Alloys Using Laser-Based Heating, JOM 68 (2016) 978–984, https://doi.org/10.1007/s11837-015-1774-0.

[15] N.P. Calta, J. Wang, A.M. Kiss, A.A. Martin, P.J. Depond, G.M. Guss, V. Thampy, A.Y. Fong, J.N. Weker, K.H. Stone, C.J. Tassone, M.J. Kramer, M.F. Toney, A. Van Buuren, M.J. Matthews, An instrument for in situ time-resolved X-ray imaging and diffraction of laser powder bed fusion additive manufacturing processes, Review of Scientific Instruments. 89 (2018) 055101, , https://doi.org/10.1063/1.5017236.

[16] C.L.A. Leung, S. Marussi, R.C. Atwood, M. Towrie, P.J. Withers, P.D. Lee, In situ X-ray imaging of defect and molten pool dynamics in laser additive manufacturing, Nature Communications. 9 (2018), https://doi.org/10.1038/s41467-018-03734-7.

[17] C. Zhao, K. Fezzaa, R.W. Cunningham, H. Wen, F. De Carlo, L. Chen, A.D. Rollett, T. Sun, Real-time monitoring of laser powder bed fusion process using high-speed X-ray imaging and diffraction, Scientific Reports. 7 (2017), https://doi.org/10.1038/s41598-017-03761-2.

[18] S. Hocine, H. Van Swygenhoven, S. Van Petegem, C.S.T. Chang, T. Maimaitiyili, G. Tinti, D. Ferreira Sanchez, D. Grolimund, N. Casati, Operando X-ray diffraction during laser 3D printing, Materials Today. (2019), https://doi.org/10.1016/j.mattod.2019.10.001.

[19] I. Gibson, D. Rosen, B. Stucker, Additive Manufacturing Technologies, Springer, New York, New York, NY, 2015, https://doi.org/10.1007/978-1-4939-2113-3.

[20] R.L. Brown, J.C. Richards, Chapter 2 - Packings, in: R.L. Brown, J.C. Richards (Eds.), Principles of Powder Mechanics, Pergamon, 1970, pp. 13–39, , https://doi.org/10.1016/B978-0-08-006605-9.50006-1.

[21] A.B. Spierings, M. Voegtlin, T. Bauer, K. Wegener, Powder flowability characterisation methodology for powder-bed-based metal additive manufacturing, Prog Addit Manuf. 1 (2016) 9–20, https://doi.org/10.1007/s40964-015-0001-4.

[22] R. Boyer, G. Welsch, E.W. Collings (Eds.), Materials properties handbook: titanium alloys, ASM International, Materials Park, Ohio, 2007.

[23] T. Ahmed, H.J. Rack, Phase transformations during cooling in α + β titanium alloys, Materials Science and Engineering: A. 243 (1998) 206–211, https://doi.org/10.1016/S0921-5093(97)00802-2.

[24] T. Vilaro, C. Colin, J.D. Bartout, As-Fabricated and Heat-Treated Microstructures of the Ti-6Al-4V Alloy Processed by Selective Laser Melting, Metall and Mat Trans A. 42 (2011) 3190–3199, https://doi.org/10.1007/s11661-011-0731-y.

[25] J. Yang, H. Yu, J. Yin, M. Gao, Z. Wang, X. Zeng, Formation and control of martensite in Ti-6Al-4V alloy produced by selective laser melting, Materials & Design. 108 (2016) 308–318, https://doi.org/10.1016/j.matdes.2016.06.117.

[26] P. Barriobero-Vila, J. Gussone, J. Haubrich, S. Sandlöbes, J. Da Silva, P. Cloetens, N. Schell, G. Requena, Inducing Stable α + β Microstructures during Selective Laser Melting of Ti-6Al-4V Using Intensified Intrinsic Heat Treatments, Materials. 10 (2017) 268, https://doi.org/10.3390/ma10030268.

[27] D.K. Do, P. Li, The effect of laser energy input on the microstructure, physical and mechanical properties of Ti-6Al-4V alloys by selective laser melting, Virtual and Physical Prototyping. 11 (2016) 41–47, https://doi.org/10.1080/17452759.2016.1142215.

[28] C. de Formanoir, A. Brulard, S. Vivès, G. Martin, F. Prima, S. Michotte, E. Rivière, A. Dolimont, S. Godet, A strategy to improve the work-hardening behavior of Ti–6Al–4V parts produced by additive manufacturing, Materials Research Letters (2016) 1–8, https://doi.org/10.1080/21663831.2016.1245681.

[29] Slic3r - Open source 3D printing toolbox, (n.d.). https://slic3r.org/ (Accessed 8 October 2019).

[30] G. Tinti, A. Bergamaschi, S. Cartier, R. Dinapoli, D. Greiffenberg, I. Johnson, J.H. Jungmann-Smith, D. Mezza, A. Mozzanica, B. Schmitt, X. Shi, Performance of the EIGER single photon counting detector, Journal of Instrumentation. 10 (2015), https://doi.org/10.1088/1748-0221/10/03/C03011 C03011–C03011.

[31] Bubble: fast powder integration - pyFAI on steroids — SNBL Software Guide 0.1 documentation, (n.d.). https://soft.snbl.eu/bubble.html (Accessed 13 February 2020).

[32] Fast Azimuthal Integration using Python — pyFAI 0.18.0a0 documentation, (n.d.). https://pyfai.readthedocs.io/en/latest/ (Accessed 13 February 2020).

[33] K.H. Harbbi, A.A. Ihsan, Studying Variance Method of X-Ray Diffraction Line Profile Then Develop It to Three New Models for Determine New Parameters, Advances in Physics Theories and Applications. 49 (2015) 46–56.